



Article

Assessment of UAV and Ground-Based Structure from Motion with Multi-View Stereo Photogrammetry in a Gullied Savanna Catchment

Jack Koci ^{1,*}, Ben Jarihani ¹, Javier X. Leon ^{1,2} , Roy C. Sidle ¹, Scott N. Wilkinson ³  and Rebecca Bartley ⁴

¹ Sustainability Research Centre, University of the Sunshine Coast, Sippy Downs 4556, QLD, Australia; bjarihan@usc.edu.au (B.J.); jleon@usc.edu.au (J.X.L.); rsidle@usc.edu.au (R.C.S.)

² School of Science and Engineering, University of the Sunshine Coast, Sippy Downs 4556, QLD, Australia

³ Land and Water, Commonwealth Scientific and Industrial Research Organisation, Canberra 2601, ACT, Australia; scott.wilkinson@csiro.au

⁴ Land and Water, Commonwealth Scientific and Industrial Research Organisation, Brisbane 4102, QLD, Australia; rebecca.bartley@csiro.au

* Correspondence: jack.koci@research.usc.edu.au; Tel.: +61-7-5456-5973

Received: 1 September 2017; Accepted: 24 October 2017; Published: 30 October 2017

Abstract: Structure from Motion with Multi-View Stereo photogrammetry (SfM-MVS) is increasingly used in geoscience investigations, but has not been thoroughly tested in gullied savanna systems. The aim of this study was to test the accuracy of topographic models derived from aerial (via Unmanned Aerial Vehicle, ‘UAV’) and ground-based (via handheld digital camera, ‘ground’) SfM-MVS in modelling hillslope gully systems in a dry-tropical savanna, and to assess the strengths and limitations of the approach at a hillslope scale and an individual gully scale. UAV surveys covered three separate hillslope gully systems (with areas of 0.412–0.715 km²), while ground surveys assessed individual gullies within the broader systems (with areas of 350–750 m²). SfM-MVS topographic models, including Digital Surface Models (DSM) and dense point clouds, were compared against RTK-GPS point data and a pre-existing airborne LiDAR Digital Elevation Model (DEM). Results indicate that UAV SfM-MVS can deliver topographic models with a resolution and accuracy suitable to define gully systems at a hillslope scale (e.g., approximately 0.1 m resolution with 0.4–1.2 m elevation error), while ground-based SfM-MVS is more capable of quantifying gully morphology (e.g., approximately 0.01 m resolution with 0.04–0.1 m elevation error). Despite difficulties in reconstructing vegetated surfaces, uncertainty as to optimal survey and processing designs, and high computational demands, this study has demonstrated great potential for SfM-MVS to be used as a cost-effective tool to aid in the mapping, modelling and management of hillslope gully systems at different scales, in savanna landscapes and elsewhere.

Keywords: Digital Elevation Model (DEM); Digital Surface Model (DSM); gully erosion; point cloud; Unmanned Aerial Vehicle (UAV)

1. Introduction

Gully erosion is a globally significant land degradation process that has detrimental environmental, ecological and economic impacts across a range of landscape systems [1–7]. Effective management of gully erosion requires high-resolution topographic information that can be used to accurately quantify the spatial distribution and density of gully systems, gully morphology and morphologic change, and the catchment characteristics that influence gully evolution [2,8–10]. Recent advances in remote sensing techniques have greatly improved our ability to collect high-resolution topographic data at a range of

scales [11–13]. Light Detection and Ranging (LiDAR), for example, has become a major source of digital terrain information [11,12,14,15], and can be deployed from both airborne (e.g., airborne laser scanning, ALS) and terrestrial (e.g., terrestrial laser scanning, TLS) platforms. A major limitation of LiDAR is the high instrument and survey costs [13]. Structure from Motion with Multi-View Stereo photogrammetry (hereafter referred to as SfM-MVS) is increasingly utilised as a cost-effective alternative method of rapidly acquiring very high resolution (sub-meter) and hyper-resolution (sub-centimetre) topographic data [13,16–19].

SfM-MVS allows the creation of three-dimensional (3D) topographic models from a set of conventional digital photographs. In addition to topographic data, SfM-MVS also produces very high resolution ortho-photo mosaics, providing a wealth of information for use in physical geography [13]. Over the past 10 years, SfM-MVS has been applied in a variety of geoscience investigations, including but not limited to; glaciology [20,21]; landslides [22,23]; volcanology [17,24]; structural geology [25]; fluvial morphology and flood reconstruction [26–29]; coastal morphology and coral reef studies [30–34]; and soil micro-topography [35–37]. SfM-MVS is also increasingly utilised in gully studies, with work conducted in: Spain [38–41]; the Iberian Peninsula [18]; Italy [42]; Morocco [43–45]; the European Loess Belt [46]; upland sites across the UK [47]; California [48] and Iowa [49,50] in the United States; Northern Ethiopia [46,51]; and China [52–54]. These studies have utilised both aerial (e.g., via Unmanned Aerial Vehicle, ‘UAV’) and ground-based (e.g., via handheld digital camera) survey techniques, but rarely are the two approaches investigated in the same study [18,41,47]. Previous studies have generally found SfM-MVS to be of comparable accuracy to equivalent LiDAR techniques, demonstrating great potential for it to be used in geomorphic investigations.

Currently, no studies have applied SfM-MVS to assess gully erosion in tropical savanna landscapes. Tropical savannas are particularly susceptible to gully erosion [9,55,56], but, compared to temperate landscapes, have received relatively little attention [3,56,57]. In this environment, accurately surveying gullies is challenging due to the complex spatial arrangement and distribution of vegetation, complex gully morphologic features (e.g., overhangs, undercuts, steep walls), and the large geographic extent in which gullies occur [15]. Gully erosion is particularly significant in the grazed dry-tropical savanna catchments tributary to the Great Barrier Reef (GBR), Australia [57–60]. In these catchments, more than 80,000 km of gully features have been identified [61], primarily on land in beef cattle production, which occupies about 75% of the total GBR catchment area (~423,000 km²) [62]. Increasing evidence suggests gully erosion on these grazing lands is the dominant source of sediments and particulate nutrients (i.e., sorbed onto sediments) to coastal waters in the region [59,63–68]. High loads of sediments and nutrients in coastal waterways are believed to be major contributing factors to the declining health of the coral reef ecosystem [58,59,69]. Gully erosion on grazed savanna landscapes is therefore a priority for management intervention [59,60,70,71].

In the GBR catchments, predictive models that relate gully density to landscape factors (e.g., geology, soil, topography, vegetation, land use) and climate have been used to quantify the extent of gully erosion at both local and regional scales [72,73]. The outputs of these models have then been used as inputs to broad scale catchment sediment budget models (Sediment River Network Model, [74–76]), to identify primary erosion processes, estimate end-of-catchment sediment loads, and inform management interventions [71,74]. A key limitation of this approach has been a lack of high-resolution topographic data to accurately quantify the extent of gully systems across the landscape [75–77]. Further, few studies have quantitatively measured gully morphology and morphologic change [56,57,78,79], leading to uncertainty about the volume and mass of sediment fractions delivered to the stream network from gully erosion [77]. Finally, understanding of the key landscape factors and processes controlling gully erosion in this environment remains limited [57,58,79–81]. Yet, this information is critical for prioritising gully erosion hotspots, understanding gully erosion processes and dynamics, and for designing, monitoring and evaluating gully remediation activities [1,2]. Addressing such data and knowledge gaps requires the utilisation of a range of topographic survey methods at various spatial and temporal scales [3,15,58].

This study tests the accuracy of topographic models derived from aerial (via UAV) and ground-based (via handheld digital camera) SfM-MVS in modelling hillslope gully systems located in a dry-tropical savanna catchment tributary to the GBR, and assesses the strengths and limitations of the approach at a hillslope scale and an individual gully scale.

2. Materials and Methods

2.1. Study Site

The study sites are located in the Weany Creek sub-catchment (13.6 km²) within the Upper Burdekin Catchment (~36,000 km²) and part of the Burdekin River Basin (130,000 km²), which drains to the GBR in northeast Australia (Figure 1). The area has granodiorite lithology [82,83] and is dominated by chromosol soil, a sandy clay loam, known locally as red goldfields soil. Chromosol soils, which cover approximately 12% of the Burdekin River basin, contain numerous gullies and are a priority for management intervention [84]. The terrain is dissected by many drainage depressions, although relief and slope gradients are low (median gradient is 2.3% [85]). The climate is dry-tropical with two distinct seasons; a summer wet season between October and March, and a dry season between April and September [86]. The mean-annual rainfall (1900–2012) is 686 mm year⁻¹, but exhibits high interannual variability linked to the phase of the Southern Oscillation, with drought conditions coinciding with El Niño/Southern Oscillation (ENSO), and wetter periods accompanying anti-ENSO (La Niña) events [87,88]. Vegetation is generally characterised by a discontinuous upper stratum of *Eucalyptus* spp. and a more continuous understory of annual and perennial grasses, forbs, and small shrubs [89] (Figure 2). Vegetation grows rapidly during the wet season, followed by a period of desiccation in the dry season [90–92]. Cattle grazing commenced in the area after 1850 and remains the dominant land use today.

Within the Weany Creek sub-catchment, measurements were focused in three separate hillslope gully systems (known as 'G1', 'G3', and 'G6'). These systems contain a diversity of gully features and ground cover conditions, considered representative of the broader sub-catchment. UAV surveys covered each hillslope system, while ground-based ('ground') surveys covered a single gully within each system (known as 'G1 gully', 'G3 gully' and 'G6 gully'). The individual gully sites were selected because they had been previously studied [57,93] and contain contrasting morphological features. The survey areas of hillslopes G1, G3, and G6 are 0.715, 0.412 and 0.451 km², respectively. The survey areas of gullies G1, G3, and G6 are 650, 350, and 750 m², respectively.

G1 gully is a V-shaped gully with steep sidewalls (45–90°), a narrow gully floor (0.2–1 m wide) and two distinct headcuts (Figure 3a). The headcuts are slightly overhanging in the upper 0.5–1 m of the incision profile, with total headcut depths ranging from 1–1.5 m. G3 gully is a U-shaped gully, with very steep sidewalls (~70–90°) ranging in height from 1 to 2.5 m, a slightly wider gully floor (1–1.5 m) and a single distinct headcut (0.5 m) that sits below a small (1 × 0.5 m deep) incised drainage depression (Figure 3b). G6 gully is more variable in shape, with sidewalls ranging from steeply dipping (45–90°) to more gently sloping (<45°), and gully bed widths ranging from 0.2–1 m. The main headcut of G6 is ~1 m deep and sits approximately 5 m below two smaller headcuts (~0.5 m deep) (Figure 3c). Evidence of mass wasting at the headcuts is clearly visible in all three gullies, with scouring around the base of the headwall, and sediment deposits on the gully floor. Rill fluting occurs along portions of gully sides. Weathered bedrock is exposed in sections of gully wall, typically in the lower 0.5 m of the profile. At the time of the ground survey (October 2016), grass (predominantly Indian Couch (*Bothriochloa pertusa*) and woody legumes (*Stylosanthes* spp.); height of ~30–50 cm) occupied much of the area along the gully edges and in some sections of the more gently sloping gully wall, obscuring the bare soil. Leaves, bark and woody debris also partially covered the ground. Grass was not present in the gully floor. Thicker pockets of low-lying shrubs (~1 m tall × 1 m wide) occupied some sections of gully edge and walls.

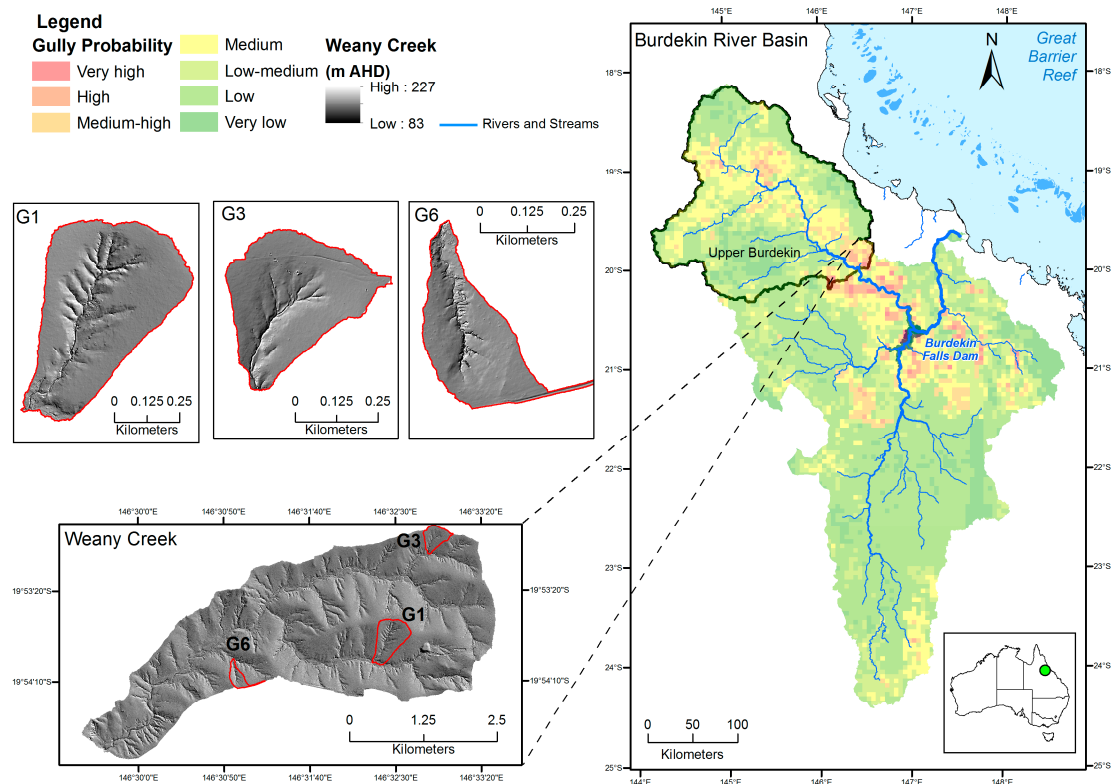


Figure 1. Map showing the location of the study sites within the Weany Creek sub-catchment, within the Upper Burdekin catchment and part of the Burdekin River Basin. The gully probability mapping is reproduced with permission from Gilad et al. [84] and shows high to very high probability of gullies in the Upper Burdekin catchment. The Weany Creek DEM and the Hillslope DEMs are derived from airborne LiDAR captured in 2013, outlined in Tindall et al. [76].

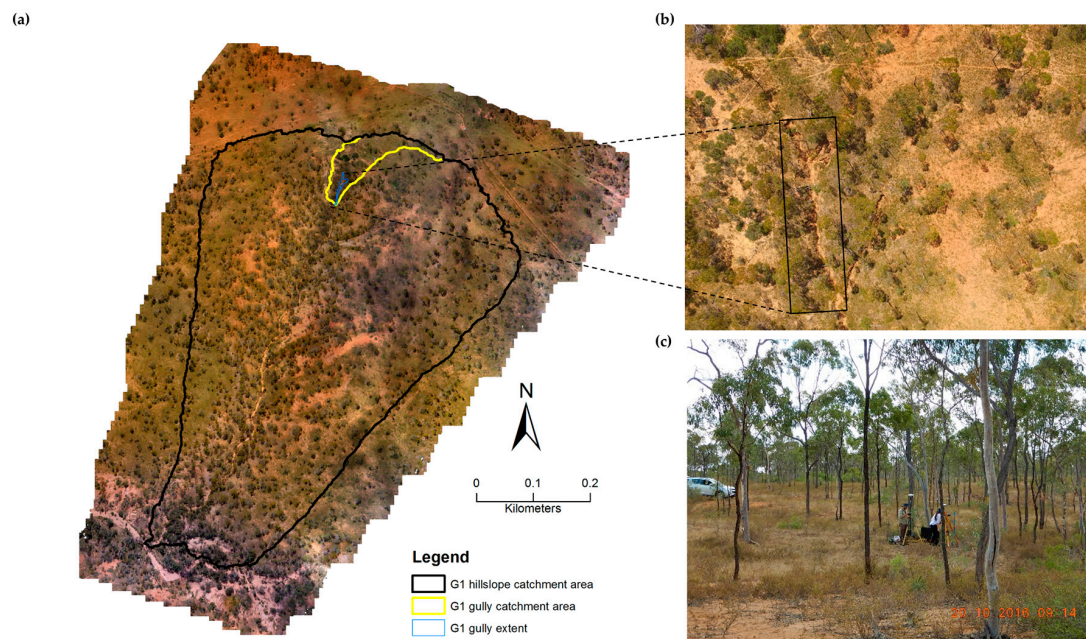


Figure 2. (a) Map showing the catchment area of G1 and the individual gully site. Background map is a UAV ortho-photo mosaic of G1. (b) UAV image of the gully site. (c) Ground image of typical savanna vegetation in the contributing area of G1.

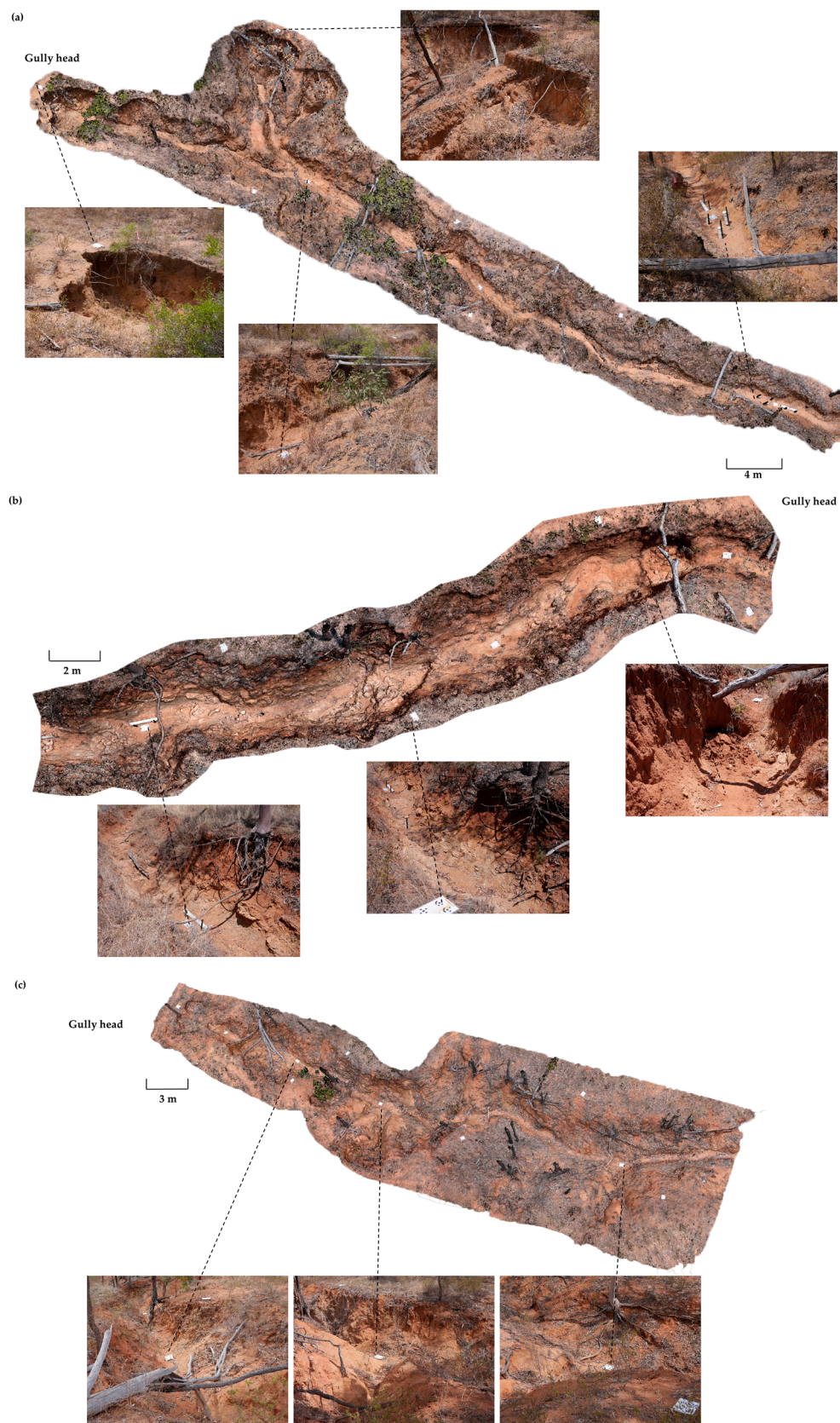


Figure 3. 3D Ground Digital Surface Model (DSM) of: (a) G1 gully; (b) G3 gully; and (c) G6 gully, with inset photographs at specific points used in SfM-MVS reconstruction. Note, the scale bar does not relate to inset photographs.

2.2. Datasets

2.2.1. LiDAR

The airborne LiDAR data, covering the area around and including the hillslope site, was acquired in 2013 as part of a larger airborne LiDAR survey campaign by the Queensland Department of Science, Information Technology, Innovation and the Arts [76]. The sensors were configured to sample the gully environment with an average pulse density of 4.2 pulses per m^2 (each pulse recorded up to five returns) and an overlap of 50% between flight runs to minimise the impact of occlusion from variable terrain and vegetation. This resulted in an average of 8 pulses per m^2 . DEM surfaces were interpolated using the natural neighbour algorithm [94] at a spatial resolution of 0.5 m using the LiDAR returns classified as ground. More detail on LiDAR capture specifications and DEM generation are given in Tindall et al. [76]. The amount of erosion across the hillslopes sites in the three years between the airborne LiDAR survey and UAV survey was minimal, due to a limited number of erosive rainfall events over this period.

2.2.2. UAV and Ground Survey

In August 2016, a UAV survey of the hillslope sites was conducted using a DJI Phantom 3 Professional Drone with photographs taken with a nadir (vertical) viewing direction [95] (Table 1). The flying mission was planned using the Map Pilot App by Maps Made Easy [96]. GPS measurements recorded by the UAV were not used in the processing of the data. Ground Control Points (GCPs) were positioned approximately in the corners and centre of each hillslope gully system catchment area, in a layout considered sufficient to adequately constrain the SfM-MVS model (Figures 4a and 6). The GCPs consisted of a 1.2×1.2 m black and white “iron cross” vinyl marker. The GCPs and a number of random validation points (used to evaluate the accuracy of the SfM-MVS topographic models), were surveyed using a CHC X91 Real Time Kinematic GPS (RTK GPS) receiver. The RTK GPS had a mean horizontal error of 0.014 m (standard deviation, SD of 0.004 m), and a mean vertical error of 0.030 m (SD of 0.010 m). Further details about the UAV survey are outlined in Table 2.

In October 2016, the ground survey of the gully sites was conducted using a Panasonic GH3 digital single-lens reflex (DSLR) camera (Table 1). No geocoding information was collected during ground photo acquisition. GCPs were distributed on the ground surface throughout the gully system along the gully edge, wall and floor (Figure 4b). The GCPs consisted of a laminated A4 page with four coded circular targets, produced using the ‘Print Markers’ tool within AgiSoft PhotoScan Professional V1.3 (PhotoScan) [97]. The GCPs and a number of random validation points were surveyed using an Ashtech Magellan Promark 500 RTK GPS. The RTK GPS had a mean horizontal error of 0.018 m (SD of 0.003 m) and a mean vertical error of 0.026 m (SD of 0.004 m). Further details about the ground survey are outlined in Table 2.

Initial attempts at the ground survey, involving significantly fewer photos and a non-systematic approach to image capture (e.g., random path of photographer, images captured non-consecutively) resulted in poor surface reconstruction. Here we outline the method of image capture found to produce the best surface reconstruction (Figure 4c,d). The photographer started at the gully head, approximately 3 m from the gully edge, and worked their way along the gully perimeter, capturing one image approximately every meter, focusing obliquely on the opposite bank toward the downstream end. Upon reaching the gully outlet, the photographer followed the same path back toward the gully head, again focusing obliquely on the opposite bank, but this time toward the upstream end. Upon reaching the gully head (i.e., the starting point), the photographer moved to the gully edge and repeated the process. Once images were captured on both sides of the gully boundary, the photographer then captured images through the centre of the gully, walking along the gully bed. Here the photographer started at the gully head and captured a series of images focused directly downstream. Upon reaching the gully outlet, the photographer followed the same path back toward the gully head, this time capturing images focused directly upstream. The photographer then repeated

this process, but changed the point of focus to be obliquely toward the left and right bank, respectively, collecting images in both the upstream and downstream direction. Following guidance provided by Smith et al. [13], the photographer tried to achieve full 360° coverage of gully features with a high degree of overlap between images; avoided large angular changes of >25–30° between adjacent camera locations and large jumps in scale; and minimised the interval between images to reduce the effect of changes in lighting and shadow conditions.

Table 1. Camera specifications.

Survey	Camera Name	Sensor	Sensor Resolution	Lens	Image Resolution	Mode
UAV	DJI FC300X	1/2.3" CMOS	12.4 MP	DJI 20 mm (35 mm format equivalent) f/2.8	12 MP	Automatic (no flash)
Ground	Panasonic GH3	4/3" CMOS	16.1 MP	Panasonic Lumix G 20 mm f/1.7 II ASPH prime	8 MP	Automatic (no flash)

Table 2. UAV and ground survey details.

System	Survey	~Altitude of Image Capture (m)	Forward Overlap (%)	Side Overlap (%)	Number of Images Captured	Image Overlap (Num. of Images)	Area Covered (m ²)	Ground Sampling Distance (cm pix ^{−1})	Number of GCPs	Number of Validation Points
G1	UAV	99	80	75	938	>9	715,000	3.31	7	151
	Ground	1.5	-	-	1747	>9	650	0.129	10	471
G3	UAV	86	80	75	451	>9	412,000	2.89	7	142
	Ground	1.5	-	-	935	>9	350	0.129	7	372
G6	UAV	97	80	75	603	>9	451,000	3.05	6	222
	Ground	1.5	-	-	1228	>9	750	0.132	10	426

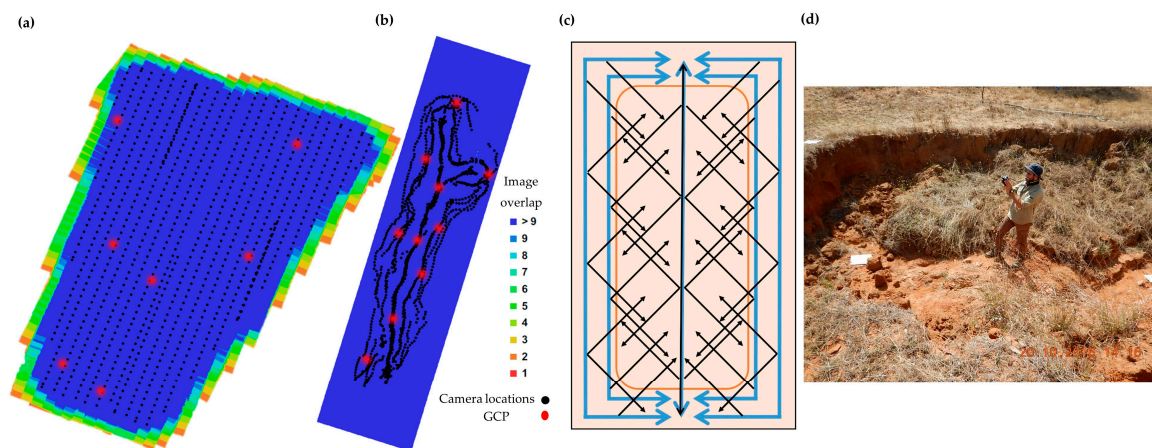


Figure 4. Camera and GCP locations and image overlap of (a) UAV survey of G1; and (b) ground survey of G1 gully; (c) theoretical path of photographer (blue arrows) and direction of image capture (black arrows) during ground survey. The brown line diagrammatically defines the gully edge. (d) Photographer during a ground survey.

2.3. Data Post-Processing

2.3.1. SfM-MVS Workflow, 3D Model, and Ortho-Photo Mosaic Generation

Agisoft PhotoScan software was used to implement the SfM-MVS workflow. Details of the processing parameters and processing times are provided in Supplementary Table S1. The SfM-MVS workflow, described in detail elsewhere [13,19], can be summarised in three main steps. The first step involves: (i) the identification and matching of features in a set of images, utilising an algorithm

based on the scale-invariant feature transform (SIFT) object recognition system [98]; and (ii) the implementation of bundle adjustment algorithms to estimate the 3D geometry (or structure) of a scene, as well as the internal and external camera orientation parameters [97], producing a sparse, unscaled 3D point cloud in arbitrary units. The second step involves: (i) a linear similarity transformation to scale and georeference the point cloud, utilising reference coordinates of GCPs distributed throughout the study site; and (ii) point cloud optimisation, a process in which camera parameters and 3D points are adjusted to minimise the sum of the reprojection error and the georeferencing error [97]. In this study the precise location of the GCPs were automatically identified by PhotoScan and manually refined where appropriate. The final step involves the implementation of multi-view stereo (MVS) image matching algorithms to build a dense 3D point cloud. An additional step can be added to the SfM-MVS workflow to generate textured 3D models and ortho-photo mosaics derived from the dense point clouds. In this study, PhotoScan processing ran on a computer that carried an 8 GB NVIDIA Quadro K5200 graphics card, two Intel Xeon CPU E5 K5200 v2 @2.5 GHZ processors, and 128 GB RAM.

2.3.2. Digital Surface Model (DSM) Generation

DSMs, derived from the dense point clouds, were generated using the ‘rasterize’ tool in CloudCompare (v2.8) [99]. The minimum elevation point at each pixel was used to model the terrain surface, as it has the greatest chance to represent the surface within vegetated areas [26]. The UAV DSMs were generated at 0.1 m pixel size, whereas the ground DSMs were generated at 0.01 m pixel size.

2.3.3. Conversion to the Australian Height Datum

The airborne LiDAR DEM elevation values were referenced to the Australian Height Datum (AHD), whereas the RTK validation points and UAV and ground DSMs had elevation values referenced to the ellipsoid GDA94. To allow comparison among the datasets, the elevation values of the DSMs and RTK validation points were converted to AHD, using the AusGeoid09 transformation [100], prior to accuracy assessment.

2.3.4. Elevation Accuracy of SfM-MVS Topographic Models

The elevation accuracy of the SfM-MVS topographic models was evaluated using point-to-raster, point-to-point, and raster-to-raster comparisons. In the point-to-raster comparison, elevation values were extracted from the DSM and compared to concordant RTK validation points. In the point-to-point comparison, elevation values were extracted from the dense point cloud (prior to rasterization) and compared to concordant RTK validation points, using the ‘compute cloud/cloud distance’ tool in CloudCompare. Point-to-point comparison is useful in topographically complex environments [101] such as gullies, where steep sides and overhangs are common [46], as a given set of x and y coordinates can have multiple z values [42,102]. In the raster-to-raster comparison, the UAV DSM was subtracted from the airborne LiDAR DEM, allowing examination of the spatial distribution of error. Here we assume the airborne LiDAR DEM is more accurate than the UAV DSM.

Elevation accuracy is evaluated for: (i) all validation points (excluding GCPs) within the hillslope sites; (ii) all validation points (excluding GCPs) within the gully sites; and (iii) individual cross-sections across the gully site. Accuracy metrics include: root mean square error (RMSE), mean absolute error (MAE), and mean error (ME) [102].

3. Results

3.1. Georeferencing Error of Ground Control Points

Georeferencing error of the GCPs is low for all gully systems and similar across survey platforms (Table 3). Total georeferencing error ranges from 0.010 to 0.027 m (0.140 to 3.351 pixels), with most of the error associated with the Z (elevation) coordinate. The high total pixel error reported for G3

ground is due to one GCP with a much higher pixel error (7.134 pixels) compared to the other GCPs (0.095 to 0.521 pixel). This GCP was not removed prior to processing in order to maintain a good distribution of GCPs over the survey area, and its inclusion did not reduce model accuracy. The low georeferencing error across all survey platforms and study sites suggests georeferencing error is not a major source of error in the SfM-MVS topographic models.

Table 3. Georeferencing error of GCPs for the UAV and ground survey. Error (m) is calculated as the root mean square error between the actual position of the GCPs, derived from RTK measurement, and the estimated position of the GCPs, derived from the SfM-MVS model. Error (pixel) is calculated as the root mean square reprojection error for the GCPs calculated over all photos where the GCPs are visible.

Coordinate Error	G1		G3		G6	
	UAV	Ground	UAV	Ground	UAV	Ground
X (m)	0.007	0.011	0.002	0.008	0.006	0.006
Y (m)	0.009	0.006	0.002	0.007	0.008	0.010
Z (m)	0.025	0.018	0.013	0.012	0.003	0.010
Total error (m)	0.027	0.022	0.013	0.016	0.010	0.015
Total error (pixels)	0.350	0.140	0.279	3.351	0.270	0.239

3.2. DSM Elevation Error

At the hillslope scale, the UAV DSM elevation error is moderate for G3 (MAE = 0.406 m), and relatively large for G6 and G1 (MAE = 0.851 and 1.220 m, respectively, Table 4). The distribution of elevation error is negatively skewed for G1 (Figure 5b) and G3 (Figure 5d), with >84% of the error between 0.5 and 3 m (i.e., the DSM is lower than the RTK validation points). In contrast, 80% of the validation points in G6 (Figure 5f) have an error of between −0.5 and −3 m (i.e., the DSM is higher than the RTK points). Comparison of the UAV dense point cloud to the RTK validation points reduced the MAE reported at the hillslope scale by 0.35, 0.16, and 0.24 m for G1, G3, G6, respectively (Table 5), suggesting some error may have been introduced during rasterization of the point cloud.

Table 4. Summary of elevation errors in the comparison of RTK validation points and UAV and ground DSMs (i.e., point-to-raster comparison).

System	Scale	RMSE (m)		MAE (m)		ME (m)	
		UAV DSM	Ground DSM	UAV DSM	Ground DSM	UAV DSM	Ground DSM
G1	Gully	1.538	0.092	1.527	0.052	1.527	−0.014
	Hillslope	1.307	NA	1.220	NA	1.180	NA
G3	Gully	0.519	0.074	0.492	0.046	0.485	−0.013
	Hillslope	0.461	NA	0.406	NA	0.326	NA
G6	Gully	0.838	0.057	0.813	0.038	−0.813	−0.015
	Hillslope	0.903	NA	0.851	NA	−0.844	NA

Table 5. Summary of the elevation errors in the comparison of RTK validation points and points extracted from UAV and ground dense point clouds (i.e., point-to-point comparison).

System	Scale	RMSE (m)		MAE (m)		ME (m)	
		UAV	Ground	UAV	Ground	UAV	Ground
G1	Gully	0.915	0.039	0.844	0.031	0.840	−0.020
	Hillslope	0.959	NA	0.870	NA	0.832	NA
G3	Gully	0.230	0.030	0.192	0.022	0.189	−0.009
	Hillslope	0.309	NA	0.244	NA	0.170	NA
G6	Gully	0.562	0.037	0.528	0.026	−0.528	−0.015
	Hillslope	0.687	NA	0.613	NA	−0.608	NA

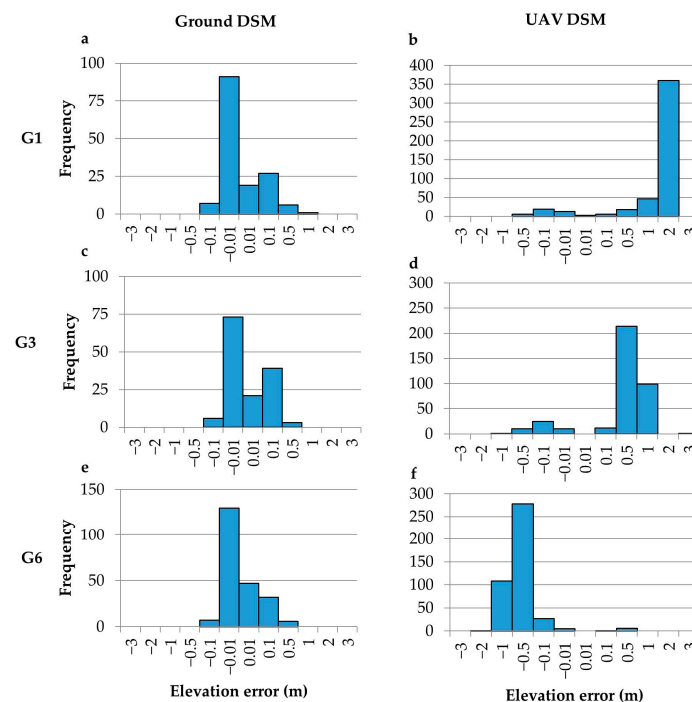


Figure 5. Distribution of elevation error (m) between RTK validation points and: (a,c,e) Ground DSM; and (b,d,f) UAV DSM, for G1, G3, and G6, respectively.

Comparison of the UAV DSM to the airborne LiDAR DEM reveals systematic error across the hillslopes, which appears to be influenced by the location of GCPs. Higher errors are observed in areas poorly constrained by GCPs. For example in G1, elevation error increases towards the centre of the upper hillslope, with increasing distance from the GCPs (Figure 6a). Similarly in G3 (Figure 6c) and G6 (Figure 6e), large portions of the hillslope have elevation errors $>1\text{m}$, corresponding to areas where there are less than three GCPs encompassing the area. It is likely that the number and distribution of GCPs across the large survey areas may have been insufficient to properly parameterize the SfM-MVS models during bundle adjustment, resulting in model deformation.

The UAV DSMs tend to underestimate terrain elevation in channelized areas (Figure 6a,c,e). This underestimation is clearly shown by comparison of cross-sections extracted from RTK points and the UAV DSM across the G1 (Figure 7b) and G3 (Figure 7d) gully sites. Here we see a negative vertical offset of around 1–1.5 m within the gully. Interestingly, examination of a cross-section in G6 gully (Figure 7f) reveals a positive vertical offset of around 0.75 m, suggesting the model behaves differently in different parts of the landscape. The amount of offset in each gully varies depending on position in the profile, being generally greater in the gully bed and smaller on the gully walls. Despite the vertical offset, all three UAV DSMs broadly follow the shape of the gully.

Vegetation is estimated to cover ~80–90% of the survey area and includes irregularly distributed grass, shrubs and trees. Visual inspection of the spatial variability of error across the ortho-photo mosaics (Figure 6b,d,f) does not reveal any distinct patterns related to vegetation effects on error; high errors are observed in both bare and vegetated patches. However, examination of the error model between the airborne LiDAR DEM and UAV DSM (particularly Figure 6c,e) clearly identify higher errors in areas corresponding to the position of dense vegetation patches (such as tree canopies and bushes). The high degree of vegetation cover at the time of survey is therefore likely to have introduced error into the UAV DSMs during image processing.

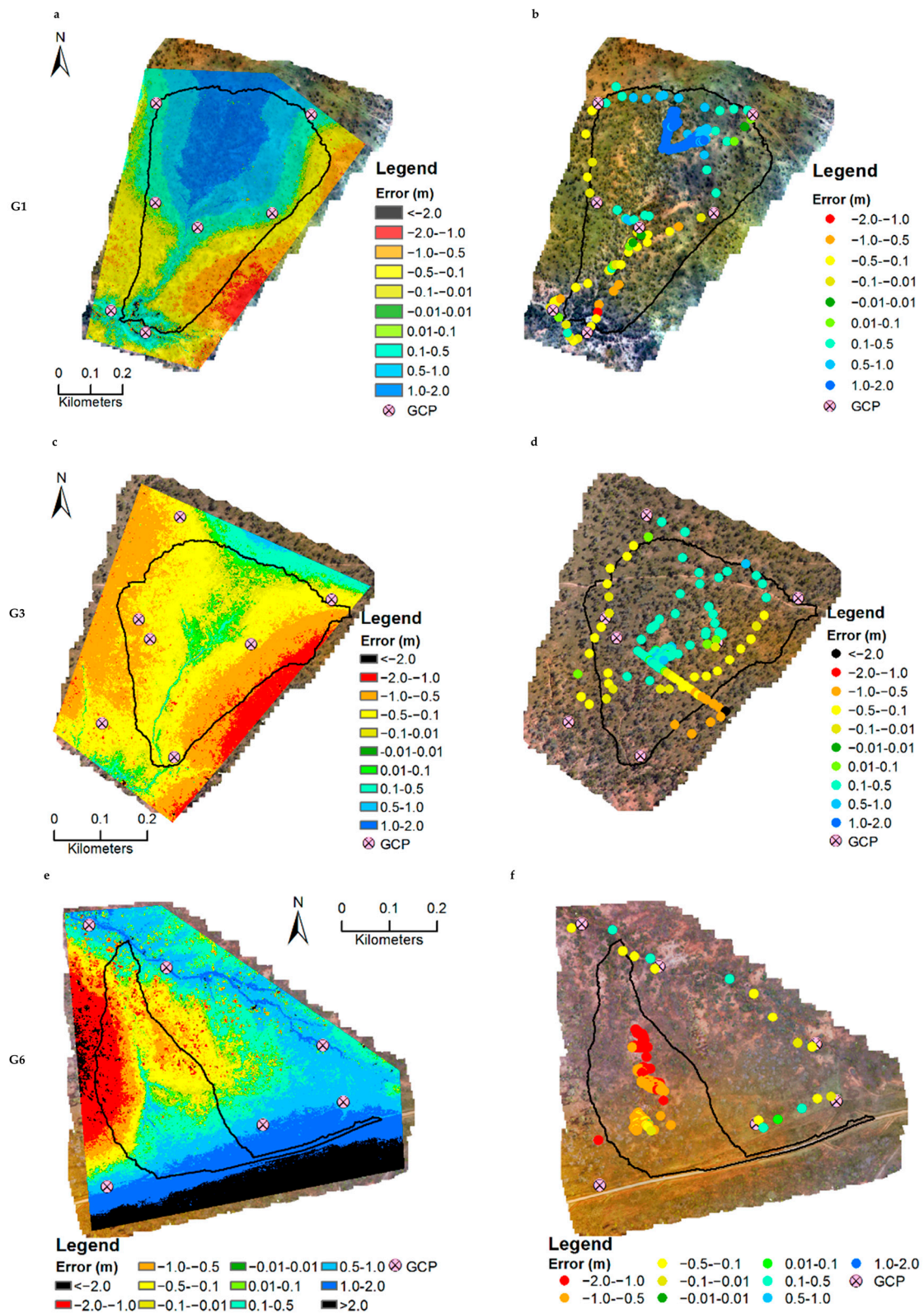


Figure 6. Map showing the difference between the airborne LiDAR DEM and the UAV DSM for (a) G1; (c) G3; and (e) G6 across the hillslope sites. Map showing the difference in elevation between RTK validation points and the UAV DSM for (b) G1; (d) G3; and (f) G6. Positive error values indicate the DSM is lower than the RTK validation point, while negative error values indicate that the DSM is higher than the RTK validation point.

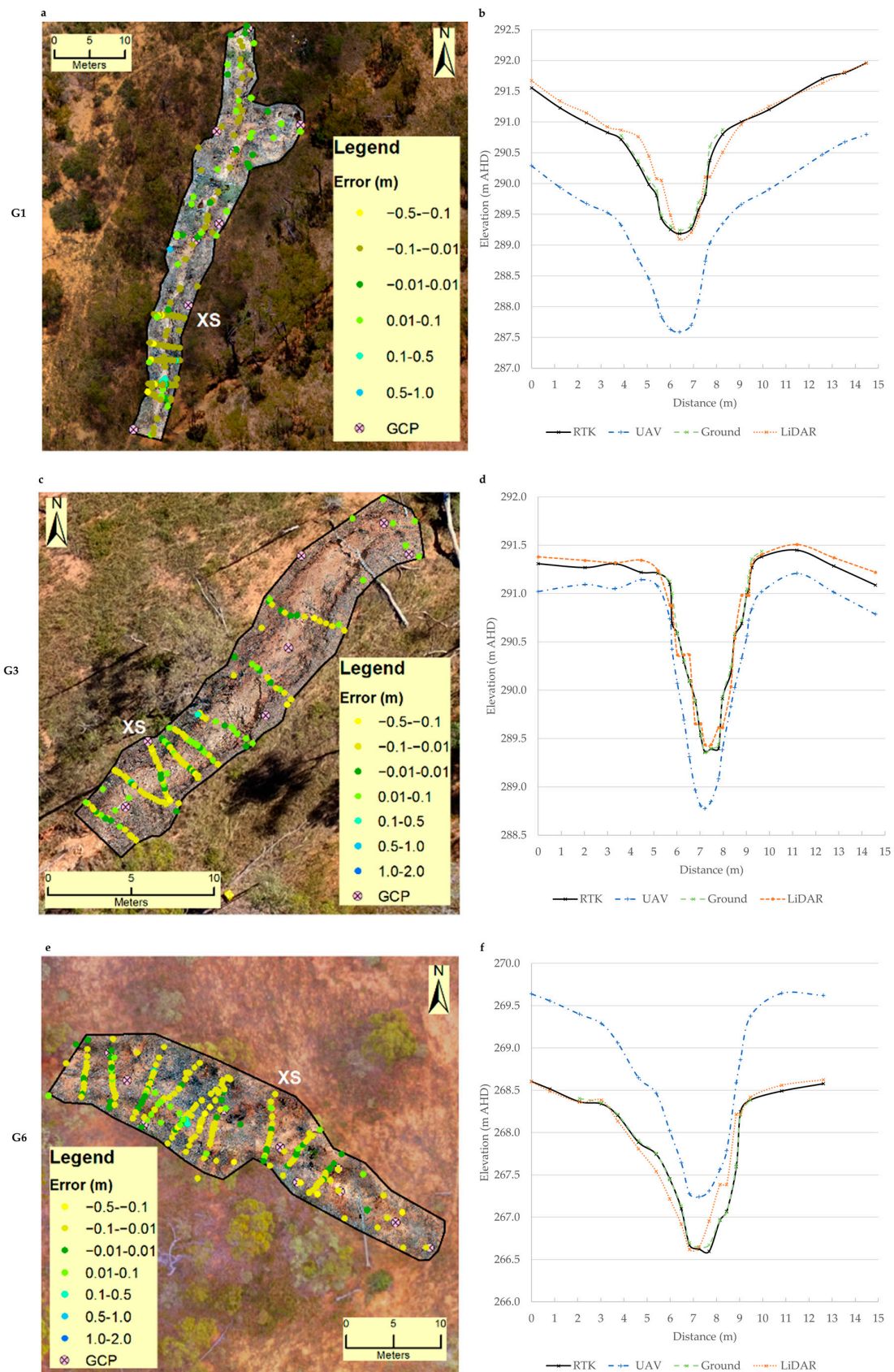


Figure 7. (a,c,e) Map showing the difference in elevation between RTK validation points and the ground DSM; and (b,d,f) comparison of cross-sectional profile between different survey platforms, for gully G1, G3, G6. Cross section locations shown on map.

At the individual gully scale, the ground DSMs have much lower elevation error (MAE = 0.052 m, 0.046 m, and 0.038 m, for G1, G3 and G6, respectively, Table 4) than the UAV DSM. The distribution of elevation error is more normally distributed for the ground DSMs with 95%, 94%, and 97% of validation points having an error of between -0.1 m and 0.1 m for G1, G3, and G6, respectively (Figure 5a,c,e). Similar to the UAV dense point cloud, comparison of the ground dense point cloud with the RTK validation dataset reduced the elevation error by 0.021, 0.024 and 0.012 m for G1, G3, and G6, respectively (Table 5), suggesting the dense point cloud better represents the complex 3D gully geometry than the DSM. No discernible pattern in elevation error related to landscape position or vegetation is apparent; errors are similar across the gully walls and gully floor, and in bare versus vegetated patches (Figure 7a,c,e). The ground DSM cross-sectional profiles closely follow the shape of the RTK profiles, providing a better representation of gully shape than the UAV DSM (Figure 7b,d,f).

3.3. Comparison of Time and Resource Requirements

The UAV surveys of the hillslope took between 3 and 4 h to complete (generally <1 h for image capture), while the ground surveys of individual gullies took between 1 to 2 h (Table 6). Processing time for ground-based images was significantly longer than for UAV images owing to the greater number of images captured and the complexity of the structures being modelled. Total time required to produce the DSMs presented in this study varied from approximately 18 to 32 h for the UAV DSMs and approximately 31 to 120 h for the ground DSMs.

Table 6. Comparison of approximate * time requirements to deliver topographic models presented in this study. Numbers in brackets represent normalised values per ha.

Area	G1		G3		G6	
	UAV SfM-MVS	Ground SfM-MVS	UAV SfM-MVS	Ground SfM-MVS	UAV SfM-MVS	Ground SfM-MVS
	71.5	0.065	41.2	0.035	45.1	0.075
Field data capture time (h) [site surveying, image capture]	4 (0.1)	2 (31)	3 (0.1)	1 (29)	3 (0.1)	2 (27)
Processing time (h) [SfM-MVS, geo-referencing, MVS, 3D model and ortho-photo mosaic generation]	24 (0.3)	90 (1385)	11 (0.3)	26 (743)	19 (0.4)	114 (1520)
Post-processing person time (h) [Data cleaning, DSM generation]	4 (0.1)	4 (62)	4 (0.1)	4 (114)	4 (0.1)	4 (53)
Total time	32 (0.4)	96 (1477)	18 (0.4)	31 (885)	26 (0.6)	120 (1600)

* As multiple gully systems were analysed on the same computer at the same time, it is difficult to accurately quantify individual processing times, thus these values should be treated as approximations only.

4. Discussion

Here we evaluate the strengths and limitations of UAV and ground SfM-MVS in modelling hillslope gully systems in tropical savannas. The strengths, limitations and opportunities are summarised in Table 7.

Table 7. Comparison of the time and resource requirements and the strengths and limitations of UAV vs. ground SfM-MVS, and opportunities for further research, as demonstrated in this study.

	UAV SfM-MVS	Ground SfM-MVS
Approximate cost of hardware [UAV, Camera + Lens, Batteries] (\$AUD)	2500	2500
Approximate cost of software (\$AUD)	550	550
Approximate time to produce final product [Field capture, processing, post-processing] (h)	18–32	~31–120
Spatial resolution (m)	0.1	0.01
Error (m)	~0.4–1.2	~0.04–0.1
Application	Cost-effective high-resolution gully and ground cover mapping at a hillslope scale (e.g., 1–100 ha).	Cost-effective very high resolution 3D modelling of gully morphology at an individual gully scale (e.g., 0.01–0.2 ha).
Strengths	<ul style="list-style-type: none"> Provides high-resolution DSMs at a hillslope scale, with elevation error comparable to, although larger than, airborne LiDAR. Provides high-resolution ortho-photo mosaics that can be used to assess ground cover (e.g., ground cover spatial arrangement, cattle trails, roads) and is valuable for land management communication. Instrument costs are very low compared to airborne LiDAR. 	<ul style="list-style-type: none"> Provides very high resolution DSMs at an individual gully scale, with elevation error comparable to TLS. Provides very high resolution 3D models that can be used to assess gully morphology and describe key erosion features. Instrument costs are very low compared to TLS.
Limitations	<ul style="list-style-type: none"> The complex structure, pattern and movement of vegetation in tropical savanna negatively affects model accuracy. The accuracy of the final topographic models strongly depends on the methodological approach implemented. There remains much uncertainty as to optimal survey and processing designs for different landscapes and geomorphological applications. The high number of images captured, mean that data storage, processing and analysis is computationally demanding. 	
Opportunities	<p>Further research is needed to:</p> <ul style="list-style-type: none"> Determine SfM-MVS survey repeatability and its ability to detect geomorphic change. Develop effective and easily applied methods of vegetation filtering from SfM-MVS datasets. Determine the optimal number and distribution of GCPs across the landscape. Determine the optimum number, overlap, height and angle of image of acquisition. 	

4.1. Strengths

4.1.1. Resolution and Accuracy

Results indicate UAV SfM-MVS can deliver topographic models with a resolution and accuracy suitable to define gully systems at a hillslope scale (e.g., ~0.1 m resolution with ~0.4–1.2 m elevation error), while ground-based SfM-MVS is more capable of quantifying gully morphology (e.g., ~0.01 m resolution with ~0.04–0.1 m elevation error). These results agree with other studies that have used aerial platforms to capture images across large areas in complex terrain (RMSE values ranging from ~0.05 m to ~1 m [18,36,47,101–103]), and ground-based approaches to model gully systems (RMSE values ranging from 0.025 m to 0.155 m [40–42,46,47,49,104,105]). While the overall elevation errors of the UAV topographic models were large relative to a pre-existing airborne LiDAR dataset and RTK validation points, cross-sections extracted from the UAV DSM broadly match the shape of gully profiles,

although are vertically offset. The elevation errors of the ground topographic models were substantially lower than those derived from UAV and are similar to those reported by recent TLS surveys of gully systems in the region [errors of ~0.05 m, 15,106]. While further work is needed to ascertain survey repeatability and the ability to detect geomorphic change [15,50,78,106], our results suggest there is great potential for both UAV and ground SfM-MVS to deliver high-resolution topographic information in gullied savanna catchments, at both the hillslope and individual gully scale.

4.1.2. Low Survey Instrument Costs and Survey Time

A major strength of SfM-MVS is the low survey instrument costs. In our study, we utilised a lightweight UAV (<2 kg) and camera (total cost including accessories was ~\$AUD 2500) to capture aerial imagery at the hillslope scale, and a DSLR camera (total cost including accessories was ~\$AUD 2500) to capture ground-based imagery at the individual gully scale. The SfM-MVS instrument costs are considerably lower than airborne LiDAR and TLS, both of which cost >\$AUD 100,000 to purchase outright or, if data are provided by an external consultant, can cost between \$AUD 1000 and 2000 per km² [106]. The low SfM-MVS survey instrument costs mean they can be purchased outright and deployed rapidly. In Australia, lightweight drones (<2 kg) can be used without a remote pilot license [107], representing a substantial cost saving of several thousand dollars. In our study, the UAV and ground surveys took approximately four and two hours of survey time, respectively, comparable to the survey times of equivalent LiDAR approaches [106]. Information generated from SfM-MVS survey therefore has the potential to enable cost-effective prioritisation of gully erosion hotspots at a hillslope scale (via aerial surveys), and to be used as a tool in the design, monitoring and evaluation of gully remediation activities at individual gully scales (via ground-based survey).

4.1.3. High-Resolution Ortho-Photo Mosaics and 3D Models

High-resolution ortho-photo mosaics and 3D models produced as part of the SfM-MVS workflow provide a wealth of additional information that can be used to improve understanding of hillslope processes and aid in gully erosion management. Visual interpretation of the 3D model of the gully site, for example, allows detailed description of gully morphology and erosion features in a more systematic way than can be achieved in the field (Figure 3). Similarly, the ortho-photo mosaics provide valuable insights into landscape factors that may influence gully development (e.g., ground cover type and spatial arrangement, cattle trails, roads). Ortho-photo mosaics and 3D models also provide excellent resources to visually communicate the benefits of improved land management to a range of stakeholders.

4.2. Limitations

4.2.1. Vegetation

Vegetation presents a significant challenge for the generation of accurate topographic models for use in environmental modelling [108]. Vegetation is particularly problematic for SfM-MVS in tropical savannas, which are characterised by a grassy understory of variable density and structure and a discontinuous layer of trees and shrubs. Vegetation obstructs the view of the ground, is prone to movement (key-point matching algorithms rely on a static scene), and has a complex structure that is difficult to reconstruct [13,101,102]. Examination of the error model between the airborne LiDAR DEM and UAV DSM clearly identify higher errors in areas corresponding to the position of dense vegetation patches (such as tree canopies and bushes). It is likely that the high ground cover at the time of survey reduced the accuracy of the topographic models as highlighted in other studies [18,26,101,103]. For example, Cook [101] found that in sparsely vegetated areas, the SfM-MVS point cloud closely matched the ground returns of LiDAR, but struggled to accurately represent ground surface in areas of denser grass, bush, and trees. Similarly, Javernick [26] reported much higher RMSE values for vegetated surfaces (0.78 m) compared to bare areas (0.17 m). We tested several methods

of vegetation classification and removal (e.g., using PhotoScan's 'classification' procedure [97,109]), resampling the point cloud at larger grid sizes where vegetation clusters are observed, extracting the minimum value within the wider area [26], and point cloud classification based on multi-scale dimensionality criteria [110]). None of these methods adequately classified vegetation across our study site. Instead, the minimum elevation value point within each pixel was used to provide the best approximation of the terrain surface within vegetated areas, acknowledging that this can sometimes result in the extraction of false elevation values as a result of point scatter below the ground surface [29]. Vegetation filtering from the SfM-MVS datasets was not the focus of this study, but is an active area of research, e.g., [111–113]. If suitable vegetation filtering methods can be developed and easily applied to SfM-MVS datasets, it will greatly enhance the ability of SfM-MVS to accurately reconstruct ground topography in densely vegetated areas.

4.2.2. Methodological Uncertainty

While implementation of the SfM-MVS workflow is relatively straightforward, the accuracy of the final topographic models depends on the methodological approach used. General guidelines for SfM-MVS surveys have been described, e.g., [18], but there remains much uncertainty as to optimal survey and processing designs for different landscapes and geomorphological conditions and applications. SfM-MVS practitioners must therefore test and adapt their methodological approach to suit their particular landscape and survey goals prior to implementing broad-scale surveys. Here we highlight two key methodological considerations, namely: the number and distribution of GCPs and the method of image capture.

The number and distribution of GCPs has a strong influence on survey time and the quality of surface reconstruction [13,19,44,102,114]. In our UAV datasets, despite very low georeferencing error of GCPs, much greater elevation errors were observed in the final topographic models. It is likely that the number and distribution of GCPs was insufficient to properly parameterize the 3D model during bundle adjustment (explained in [18]). While a minimum of three GCPs are required to account for model rotation, translation, and scale during the implementation of bundle adjustment algorithms, research suggests that collection of more GCPs is better and these should adequately cover the area of interest [17,44,115,116]. Specific GCP requirements will, however, vary depending on site characteristics, quality of the image network used in surface reconstruction, and required accuracy of the final topographic model [19,44]. Given the effect of GCPs on surface reconstruction quality and the considerable field effort required to collect them, determining the optimal number and distribution of GCPs remains an important research priority.

The method of image capture also has a strong bearing on survey and processing time and the quality of surface reconstruction. During our UAV survey for example, images were captured at a height of ~85–100 m above the ground, with a single nadir (vertical) viewing direction, and a single orthographic grid flight path. This flight strategy was selected as it provided a good compromise between the extent of the survey area covered and survey time, but may have contributed to the error observed in the UAV topographic models. Recent studies have reported a decrease in model accuracy with increasing survey distance [18,19] and also demonstrated that using vertical imagery alone can introduce systematic broad-scale error into topographic models, expressed as vertical 'doming' [44,115,117]. The addition of convergent (non-nadir) imagery into aerial surveys has recently been shown to improve model accuracy [18,115]. Similarly, the addition of a second set of perpendicular flight lines (e.g., in a 'double-grid' pattern), is increasingly utilised in UAV topographic surveys to provide better image overlap and coverage of the area of interest and thus improve model performance [118]. Further testing to determine the optimum number, overlap, height and angle of image of acquisition, appropriate for both hillslope and individual gully surveys, would enable faster and more efficient survey and processing time and help to improve model accuracy. It is also important to consider the camera sensor used to capture images. Most light-weight consumer UAVs, including the DJI Phantom 3 Professional, come equipped with a rolling shutter camera, which is prone to image

distortion when images are recorded from a moving platform [119]. This may have introduced further error into our UAV topographic models. Cameras equipped with global shutters can mitigate this problem and should be considered in future UAV surveys.

4.2.3. Computational Demands

The high number and resolution of images captured during SfM-MVS surveys means that data storage, processing, and analysis is computationally demanding. For example, data from the UAV and ground survey took approximately 11–24 h and 26–114 h, respectively, to process on a computer with 8 GB graphics card, two CPU cores, and 128 GB RAM. Such computational demands may limit the scale at which SfM-MVS is currently applied and to practitioners who have access to high-performance computers. However, rapid advances in computing capability, for example, through improvements to Graphics Processing Units and the implementation of parallel computing, are revolutionizing SfM-MVS workflows [19]. As high-performance computers become more readily available, broader-scale implementation of both aerial and ground-based SfM-MVS approaches can be expected.

5. Conclusions

Structure from Motion with Multi-View Stereo photogrammetry (SfM-MVS) is increasingly used as a cost-effective method of rapidly acquiring high-resolution topographic data across a range of scales and in diverse landscapes and geomorphic settings, but has not been thoroughly tested in savanna systems. Results from our study, conducted in a gullied dry-tropical savanna catchment in Upper Burdekin catchment, indicate UAV SfM-MVS can deliver topographic models with a resolution and accuracy suitable to define gully systems at a hillslope scale (e.g., ~0.1 m resolution with ~0.4–1.2 m elevation error), while ground-based SfM-MVS is more capable of quantifying individual gully morphology (e.g., ~0.01 m resolution with ~0.04–0.1 m elevation error). High-resolution 3D topographic models and ortho-photo mosaics produced as part of the SfM-MVS workflow allow detailed description of gully morphology and contributing area characteristics (e.g., ground cover type and spatial arrangement), providing valuable information for land management and restoration practices. Modest survey instrument costs (<\$AUD 3000) and rapid survey times (~4 and 2 h for UAV and ground survey respectively) mean that SfM-MVS is highly cost-effective compared to equivalent Light Detection and Ranging (LiDAR) techniques. While SfM-MVS offers great potential, this study has also identified some important limitations of the methodology. For example, accurately reconstructing ground topography in densely vegetated areas, common across tropical savanna landscapes, remains a major challenge for SfM-MVS workflows and requires the development of improved vegetation filtering methods. There remains uncertainty as to optimal survey and processing designs to achieve the best model accuracy and reduce processing times. Finally, high computational demands for image processing may limit the spatial scale at which SfM-MVS is currently implemented and the number of practitioners who can apply it. However, as high-performance computing becomes more readily available, broader-scale application of SfM-MVS is expected. Overall, this study has demonstrated great potential for SfM-MVS to be used as a cost-effective tool to aid in the mapping, modelling, and management of complex hillslope gully systems at different scales in tropical savanna landscapes and elsewhere.

Supplementary Materials: The following are available online at www.mdpi.com/2220-9964/6/11/328/s1. Table S1: PhotoScan processing parameters and approximate times for UAV and Ground survey datasets.

Acknowledgments: This project was supported by: the Australian Government Australian Postgraduate Awards (APA) program; a Meat and Livestock Australia (MLA) Postgraduate Award; and a Commonwealth Scientific and Industrial Research Organisation (CSIRO) Postgraduate Scholarship. Funds from these sources were used to cover the costs of publishing in open access. The LiDAR DEM of Weany Creek was provided by Dan Tindall (Queensland Department of Science, Information Technology and Innovation). Anne Henderson (CSIRO) aided in the preparation of Figure 1. We gratefully acknowledge Rob and Sue Benetto of Virginia Park Station for allowing

access onto their property to undertake this work, and the two anonymous reviewers who provided comments on early versions of this manuscript.

Author Contributions: Jack Koci conceived and designed the study, collected and analysed the data, and wrote the manuscript. Ben Jarihani, Javier Leon and Roy Sidle provided input into the design of the study, aided in data collection and in the interpretation of the results, and provided input into the writing of the manuscript. Scott Wilkinson and Rebecca Bartley aided in the design of the study, assisted in the interpretation of the results, and provided input into the writing of the manuscript.

Conflicts of Interest: The authors declare no conflict of interest.

References

1. Poesen, J.; Nachtergaele, J.; Verstraeten, G.; Valentin, C. Gully erosion and environmental change: Importance and research needs. *CATENA* **2003**, *50*, 91–133. [\[CrossRef\]](#)
2. Valentin, C.; Poesen, J.; Li, Y. Gully erosion: Impacts, factors and control. *CATENA* **2005**, *63*, 132–153. [\[CrossRef\]](#)
3. Castillo, C.; Gómez, J.A. A century of gully erosion research: Urgency, complexity and study approaches. *Earth-Sci. Rev.* **2016**, *160*, 300–319. [\[CrossRef\]](#)
4. Poesen, J.; Vanwalleghe, T.; de Vente, J.; Knapen, A.; Verstraeten, G.; Martínez-Casasnovas, J.A. Gully erosion in Europe. In *Soil Erosion in Europe*; Wiley: West Sussex, UK, 2006; pp. 515–536.
5. Olley, J.M.; Wasson, R.J. Changes in the flux of sediment in the upper murrumbidgee catchment, southeastern Australia, since European settlement. *Hydrol. Process.* **2003**, *17*, 3307–3320. [\[CrossRef\]](#)
6. Wilson, G.V.; Cullum, R.F.; Römkens, M.J.M. Ephemeral gully erosion by preferential flow through a discontinuous soil-pipe. *CATENA* **2008**, *73*, 98–106. [\[CrossRef\]](#)
7. Zhao, J.; Vanmaercke, M.; Chen, L.; Govers, G. Vegetation cover and topography rather than human disturbance control gully density and sediment production on the Chinese loess plateau. *Geomorphology* **2016**, *274*, 92–105. [\[CrossRef\]](#)
8. Betts, H.D.; Trustrum, N.A.; Rose, R.C.D. Geomorphic changes in a complex gully system measured from sequential digital elevation models, and implications for management. *Earth Surf. Process. Landf.* **2003**, *28*, 1043–1058. [\[CrossRef\]](#)
9. Lal, R. Restoring land degraded by gully erosion in the tropics. In *Advances in Soil Science: Soil Restoration*; Lal, R., Stewart, B.A., Cronk, J.K., Eds.; Springer: New York, NY, USA; Berlin, Germany, 1992; Volume 17, pp. 123–152.
10. Vanmaercke, M.; Poesen, J.; Van Mele, B.; Demuzere, M.; Bruynseels, A.; Golosov, V.; Bezerra, J.F.R.; Bolysov, S.; Dvinskiy, A.; Frankl, A.; et al. How fast do gully headcuts retreat? *Earth Sci. Rev.* **2016**, *154*, 336–355. [\[CrossRef\]](#)
11. Liu, X. Airborne lidar for DEM generation: Some critical issues. *Prog. Phys. Geogr.* **2008**, *32*, 31–49. [\[CrossRef\]](#)
12. Telling, J.; Lyda, A.; Hartzell, P.; Glennie, C. Review of earth science research using terrestrial laser scanning. *Earth Sci. Rev.* **2017**, *169*, 35–68. [\[CrossRef\]](#)
13. Smith, M.W.; Carrivick, J.L.; Quincey, D.J. Structure from motion photogrammetry in physical geography. *Prog. Phys. Geogr.* **2015**, 1–29. [\[CrossRef\]](#)
14. Perroy, R.L.; Bookhagen, B.; Asner, G.P.; Chadwick, O.A. Comparison of gully erosion estimates using airborne and ground-based lidar on Santa Cruz Island, California. *Geomorphology* **2010**, *118*, 288–300. [\[CrossRef\]](#)
15. Goodwin, N.R.; Armston, J.; Stiller, I.; Muir, J. Assessing the repeatability of terrestrial laser scanning for monitoring gully topography: A case study from Aratula, Queensland, Australia. *Geomorphology* **2016**, *262*, 24–36. [\[CrossRef\]](#)
16. Westoby, M.J.; Brasington, J.; Glasser, N.F.; Hambrey, M.J.; Reynolds, J.M. ‘Structure-from-motion’ photogrammetry: A low-cost, effective tool for geoscience applications. *Geomorphology* **2012**, *179*, 300–314. [\[CrossRef\]](#)
17. James, M.R.; Robson, S. Straightforward reconstruction of 3D surfaces and topography with a camera: Accuracy and geoscience application. *J. Geophys. Res. Earth Surf.* **2012**, *117*, F03017. [\[CrossRef\]](#)
18. Smith, M.W.; Vericat, D. From experimental plots to experimental landscapes: Topography, erosion and deposition in sub-humid badlands from structure-from-motion photogrammetry. *Earth Surf. Process. Landf.* **2015**, *40*, 1656–1671. [\[CrossRef\]](#)

19. Eltner, A.; Kaiser, A.; Castillo, C.; Rock, G.; Neugirg, F.; Abellán, A. Image-based surface reconstruction in geomorphometry—Merits, limits and developments. *Earth Surf. Dyn.* **2016**, *4*, 359–389. [[CrossRef](#)]
20. Piermattei, L.; Carturan, L.; Guarnieri, A. Use of terrestrial photogrammetry based on structure-from-motion for mass balance estimation of a small glacier in the Italian Alps. *Earth Surf. Process. Landf.* **2015**, *40*, 1791–1802. [[CrossRef](#)]
21. Gómez-Gutiérrez, Á.; de Sanjosé-Blasco, J.; de Matías-Bejarano, J.; Berenguer-Sempere, F. Comparing two photo-reconstruction methods to produce high density point clouds and DEMs in the Corral del Veleta rock glacier (Sierra Nevada, Spain). *Remote Sens.* **2014**, *6*, 5407–5427. [[CrossRef](#)]
22. Stumpf, A.; Malet, J.P.; Allemand, P.; Pierrot-Deseilligny, M.; Skupinski, G. Ground-based multi-view photogrammetry for the monitoring of landslide deformation and erosion. *Geomorphology* **2015**, *231*, 130–145. [[CrossRef](#)]
23. Lucieer, A.; de Jong, S.; Turner, D. Mapping landslide displacements using structure from motion (SfM) and image correlation of multi-temporal UAV photography. *Prog. Phys. Geogr.* **2013**, 97–116. [[CrossRef](#)]
24. James, M.R.; Varley, N. Identification of structural controls in an active lava dome with high resolution DEMs: Volcán de Colima, Mexico. *Geophys. Res. Lett.* **2012**, *39*, L22303. [[CrossRef](#)]
25. Bemis, S.P.; Micklethwaite, S.; Turner, D.; James, M.R.; Akciz, S.; Thiele, S.T.; Bangash, H.A. Ground-based and UAV-based photogrammetry: A multi-scale, high-resolution mapping tool for structural geology and paleoseismology. *J. Struct. Geol.* **2014**, *69*, 163–178. [[CrossRef](#)]
26. Javernick, L.; Brasington, J.; Caruso, B. Modeling the topography of shallow braided rivers using structure-from-motion photogrammetry. *Geomorphology* **2014**, *213*, 166–182. [[CrossRef](#)]
27. Dietrich, J.T. Riverscape mapping with helicopter-based structure-from-motion photogrammetry. *Geomorphology* **2016**, *252*, 144–157. [[CrossRef](#)]
28. Woodget, A.S.; Carbonneau, P.E.; Visser, F.; Maddock, I.P. Quantifying submerged fluvial topography using hyperspatial resolution UAV imagery and structure from motion photogrammetry. *Earth Surf. Process. Landf.* **2015**, *40*, 47–64. [[CrossRef](#)]
29. Smith, M.W.; Carrivick, J.L.; Hooke, J.; Kirkby, M.J. Reconstructing flash flood magnitudes using ‘structure-from-motion’: A rapid assessment tool. *J. Hydrol.* **2014**, *519*, 1914–1927. [[CrossRef](#)]
30. Mancini, F.; Dubbini, M.; Gattelli, M.; Stecchi, F.; Fabbri, S.; Gabbianelli, G. Using unmanned aerial vehicles (UAV) for high-resolution reconstruction of topography: The structure from motion approach on coastal environments. *Remote Sens.* **2013**, *5*, 6880. [[CrossRef](#)]
31. Bryson, M.; Johnson-Roberson, M.; Murphy, R.J.; Bongiorno, D. Kite aerial photography for low-cost, ultra-high spatial resolution multi-spectral mapping of intertidal landscapes. *PLoS ONE* **2013**, *8*, e73550. [[CrossRef](#)] [[PubMed](#)]
32. Figueira, W.; Ferrari, R.; Weatherby, E.; Porter, A.; Hawes, S.; Byrne, M. Accuracy and precision of habitat structural complexity metrics derived from underwater photogrammetry. *Remote Sens.* **2015**, *7*, 15859–16900. [[CrossRef](#)]
33. Leon, J.X.; Roelfsema, C.M.; Saunders, M.I.; Phinn, S.R. Measuring coral reef terrain roughness using ‘structure-from-motion’ close-range photogrammetry. *Geomorphology* **2015**, *242*, 21–28. [[CrossRef](#)]
34. Brunier, G.; Fleury, J.; Anthony, E.J.; Gardel, A.; Dussouillez, P. Close-range airborne structure-from-motion photogrammetry for high-resolution beach morphometric surveys: Examples from an embayed rotating beach. *Geomorphology* **2016**, *261*, 76–88. [[CrossRef](#)]
35. Nouwakpo, S.K.; Weltz, M.A.; McGwire, K. Assessing the performance of structure-from-motion photogrammetry and terrestrial lidar for reconstructing soil surface microtopography of naturally vegetated plots. *Earth Surf. Process. Landf.* **2016**, *41*, 308–322. [[CrossRef](#)]
36. Ouédraogo, M.M.; Degre, A.; Debouche, C.; Lisein, J. The evaluation of unmanned aerial system-based photogrammetry and terrestrial laser scanning to generate DEMs of agricultural watersheds. *Geomorphology* **2014**, *214*, 339–355. [[CrossRef](#)]
37. Nouwakpo, S.K.; James, M.R.; Weltz, M.A.; Huang, C.H.; Chagas, I.; Lima, L. Evaluation of structure from motion for soil microtopography measurement. *Photogramm. Rec.* **2014**, *29*, 297–316. [[CrossRef](#)]
38. Castillo, C.; James, M.; Redel-Macías, M.; Pérez, R.; Gómez, J. Sf3m software: 3-D photo-reconstruction for non-expert users and its application to a gully network. *Soil* **2015**, *1*, 583–594. [[CrossRef](#)]
39. Castillo, C.; Taguas, E.V.; Zarco-Tejada, P.; James, M.R.; Gómez, J.A. The normalized topographic method: An automated procedure for gully mapping using GIS. *Earth Surf. Process. Landf.* **2014**, *39*, 2002–2015. [[CrossRef](#)]

40. Gómez-Gutiérrez, Á.; Schnabel, S.; Berenguer-Sempere, F.; Lavado-Contador, F.; Rubio-Delgado, J. Using 3d photo-reconstruction methods to estimate gully headcut erosion. *CATENA* **2014**, *120*, 91–101. [[CrossRef](#)]
41. Stöcker, C.; Eltner, A.; Karrasch, P. Measuring gullies by synergetic application of uav and close range photogrammetry—A case study from andalusia, spain. *CATENA* **2015**, *132*, 1–11. [[CrossRef](#)]
42. Di Stefano, C.; Ferro, V.; Palmeri, V.; Pampalone, V.; Agnello, F. Testing the use of an image-based technique to measure gully erosion at sparacia experimental area. *Hydrol. Process.* **2017**, *31*, 573–585. [[CrossRef](#)]
43. D'Oleire-Oltmanns, S.; Marzolf, I.; Peter, K.; Ries, J. Unmanned Aerial Vehicle (UAV) for monitoring soil erosion in morocco. *Remote Sens.* **2012**, *4*, 3390. [[CrossRef](#)]
44. James, M.R.; Robson, S.; d'Oleire-Oltmanns, S.; Niethammer, U. Optimising uav topographic surveys processed with structure-from-motion: Ground control quality, quantity and bundle adjustment. *Geomorphology* **2017**, *280*, 51–66. [[CrossRef](#)]
45. Peter, K.D.; d'Oleire-Oltmanns, S.; Ries, J.B.; Marzolf, I.; Ait Hssaine, A. Soil erosion in gully catchments affected by land-levelling measures in the sous basin, morocco, analysed by rainfall simulation and uav remote sensing data. *CATENA* **2014**, *113*, 24–40. [[CrossRef](#)]
46. Frankl, A.; Stal, C.; Abraha, A.; Nyssen, J.; Rieke-Zapp, D.; De Wulf, A.; Poesen, J. Detailed recording of gully morphology in 3D through image-based modelling. *CATENA* **2015**, *127*, 92–101. [[CrossRef](#)]
47. Glendell, M.; McShane, G.; Farrow, L.; James, M.R.; Quinton, J.; Anderson, K.; Evans, M.; Benaud, P.; Rawlins, B.; Morgan, D.; et al. Testing the utility of structure-from-motion photogrammetry reconstructions using small unmanned aerial vehicles and ground photography to estimate the extent of upland soil erosion. *Earth Surf. Process. Landf.* **2017**. [[CrossRef](#)]
48. Christian, P.; Davis, J. Hillslope gully photogeomorphology using structure-from-motion. *Z. Geomorphol. Suppl. Issues* **2016**, *60*, 59–78. [[CrossRef](#)]
49. Gesch, K.R.; Wells, R.R.; Cruse, R.M.; Momm, H.G.; Dabney, S.M. Quantifying uncertainty of measuring gully morphological evolution with close-range digital photogrammetry. *Soil Sci. Soc. Am. J.* **2015**, *79*, 650–659. [[CrossRef](#)]
50. Wells, R.R.; Momm, H.G.; Castillo, C. Quantifying uncertainty in high-resolution remotely sensed topographic surveys for ephemeral gully channel monitoring. *Earth Surf. Dyn.* **2017**, *5*, 347–367. [[CrossRef](#)]
51. Lannoeye, W.; Stal, C.; Guyassa, E.; Zenebe, A.; Nyssen, J.; Frankl, A. The use of sfm-photogrammetry to quantify and understand gully degradation at the temporal scale of rainfall events: An example from the ethiopian drylands. *Phys. Geogr.* **2016**, *37*, 430–451. [[CrossRef](#)]
52. Liu, K.; Ding, H.; Tang, G.; Na, J.; Huang, X.; Xue, Z.; Yang, X.; Li, F. Detection of catchment-scale gully-affected areas using unmanned Aerial Vehicle (UAV) on the chinese loess plateau. *ISPRS Int. J. Geo-Inf.* **2016**, *5*, 238. [[CrossRef](#)]
53. Wang, R.; Zhang, S.; Pu, L.; Yang, J.; Yang, C.; Chen, J.; Guan, C.; Wang, Q.; Chen, D.; Fu, B.; et al. Gully erosion mapping and monitoring at multiple scales based on multi-source remote sensing data of the sancha river catchment, northeast china. *ISPRS Int. J. Geo-Inf.* **2016**, *5*, 200. [[CrossRef](#)]
54. Zhang, B.; Xiong, D.; Su, Z.; Yang, D.; Dong, Y.; Xiao, L.; Zhang, S.; Shi, L. Effects of initial step height on the headcut erosion of bank gullies: A case study using a 3d photo-reconstruction method in the dry-hot valley region of southwest china. *Phys. Geogr.* **2016**, *37*, 409–429. [[CrossRef](#)]
55. Meadows, M.E.; Thomas, D.S.G. Tropical savannas. In *Geomorphology and Global Environmental Change*; Slaymaker, O., Spencer, T., Embleton-Hamann, C., Eds.; Cambridge University Press: Cambridge, UK, 2009; pp. 248–275.
56. Brooks, A.; Spencer, J.; Knight, J. Alluvial gully erosion: An example from the mitchell fluvial megafan, Queensland, Australia. *Earth Surf. Process. Landf.* **2009**, *34*, 43–48. [[CrossRef](#)]
57. Bartley, R.; Hawdon, A.; Post, D.A.; Roth, C.H. A sediment budget for a grazed semi-arid catchment in the Burdekin Basin, Australia. *Geomorphology* **2007**, *87*, 302–321. [[CrossRef](#)]
58. Bartley, R.; Bainbridge, Z.T.; Lewis, S.E.; Kroon, F.J.; Wilkinson, S.N.; Brodie, J.E.; Silburn, D.M. Relating sediment impacts on coral reefs to watershed sources, processes and management: A review. *Sci. Total Environ.* **2014**, *468–469*, 1138–1153. [[CrossRef](#)] [[PubMed](#)]
59. Brodie, J.; Waterhouse, J.; Schaffelke, B.; Kroon, F.; Thorburn, P.; Rolfe, J.; Johnson, J.; Fabricius, K.; Lewis, S.; Devlin, M.; et al. 2013 Scientific Consensus Statement: Land Use Impacts on Great Barrier Reef Water Quality and Ecosystem Condition; The State of Queensland: Brisbane, Australia, 2013.

60. Kroon, F.J.; Thorburn, P.; Schaffelke, B.; Whitten, S. Towards protecting the Great Barrier Reef from land-based pollution. *Glob. Chang. Biol.* **2016**, *22*, 1985–2002. [[CrossRef](#)] [[PubMed](#)]
61. Thorburn, P.J.; Wilkinson, S.N. Conceptual frameworks for estimating the water quality benefits of improved agricultural management practices in large catchments. *Agric. Ecosyst. Environ.* **2013**, *180*, 192–209. [[CrossRef](#)]
62. Waters, D.; Carroll, C.; Ellis, R.; Hateley, L.; McCloskey, G.; Packett, R.; Dougall, C.; Fentie. *Modelling Reductions of Pollutant Loads Due to Improved Management Practices in the Great Barrier Reef Catchments—Whole of Gbr*; Queensland Department of Natural Resources and Mines: Toowoomba, Australia, 2014.
63. Caitcheon, G.G.; Olley, J.M.; Pantus, F.; Hancock, G.; Leslie, C. The dominant erosion processes supplying fine sediment to three major rivers in tropical Australia, the Daly (nt), Mitchell (qld) and Flinders (qld) rivers. *Geomorphology* **2012**, *151–152*, 188–195. [[CrossRef](#)]
64. Hughes, A.O.; Olley, J.M.; Croke, J.C.; McKergow, L.A. Sediment source changes over the last 250 years in a dry-tropical catchment, central Queensland, Australia. *Geomorphology* **2009**, *104*, 262–275. [[CrossRef](#)]
65. Tims, S.G.; Everett, S.E.; Fifield, L.K.; Hancock, G.J.; Bartley, R. Plutonium as a tracer of soil and sediment movement in the herbert river, Australia. *Nucl. Instrum. Methods Phys. Res. B* **2010**, *268*, 1150–1154. [[CrossRef](#)]
66. Wasson, R.J.; Furlonger, L.; Parry, D.; Pietsch, T.; Valentine, E.; Williams, D. Sediment sources and channel dynamics, daly river, northern Australia. *Geomorphology* **2010**, *114*, 161–174. [[CrossRef](#)]
67. Olley, J.; Brooks, A.; Spencer, J.; Pietsch, T.; Borombovits, D. Subsoil erosion dominates the supply of fine sediment to rivers draining into princess charlotte bay, Australia. *J. Environ. Radioact.* **2013**, *124*, 121–129. [[CrossRef](#)] [[PubMed](#)]
68. Furuichi, T.; Olley, J.; Wilkinson, S.; Lewis, S.; Bainbridge, Z.; Burton, J. Paired geochemical tracing and load monitoring analysis for identifying sediment sources in a large catchment draining into the Great Barrier Reef Lagoon. *Geomorphology* **2016**, *266*, 41–52. [[CrossRef](#)]
69. Fabricius, K.E. Effects of terrestrial runoff on the ecology of corals and coral reefs: Review and synthesis. *Mar. Pollut. Bull.* **2005**, *50*, 125–146. [[CrossRef](#)] [[PubMed](#)]
70. Brodie, J.E.; Lewis, S.E.; Collier, C.J.; Wooldridge, S.; Bainbridge, Z.T.; Waterhouse, J.; Rasheed, M.A.; Honchin, C.; Holmes, G.; Fabricius, K. Setting ecologically relevant targets for river pollutant loads to meet marine water quality requirements for the Great Barrier Reef, Australia: A preliminary methodology and analysis. *Ocean Coast. Manag.* **2017**, *143*, 136–147. [[CrossRef](#)]
71. Wilkinson, S.N.; Bartley, R.; Hairsine, P.B.; Bui, E.N.; Gregory, L.; Henderson, A.E. *Managing Gully Erosion as an Efficient Approach to Improving Water Quality in the Great Barrier Reef Lagoon*; Report to the Department of the Environment; CSIRO Land and Water: Canberra, Australia, 2015.
72. Hughes, A.; Prosser, P.; Stevenson, J.; Scott, A.; Lu, H.; Gallant, J.; Moran, C. *Gully Erosion Mapping for the National Land and Water Audit*; Technical Report 26/01; CSIRO Land and Water: Canberra, Australia, 2001.
73. Kuhnert, P.; Kinsey-Henderson, A.; Bartley, R.; Herr, A. Incorporating uncertainty in gully erosion calculations using the random forests modelling approach. *Environmetrics* **2010**, *21*, 493–509. [[CrossRef](#)]
74. McKergow, L.A.; Prosser, I.P.; Hughes, A.O.; Brodie, J. Sources of sediment to the great barrier reef world heritage area. *Mar. Pollut. Bull.* **2005**, *51*, 200–211. [[CrossRef](#)] [[PubMed](#)]
75. Waters, D.; Carroll, C.; Ellis, R.; McCloskey, G.; Hateley, L.; Packett, B.; Dougall, C.; Fentie, B. Catchment modelling scenarios to inform gbr water quality targets. In Proceedings of the 20th International Congress on Modelling and Simulation, Adelaide, Australia, 1–6 December 2013.
76. Tindall, D.; Marchand, B.; Gilad, U.; Goodwin, N.; Denham, R.; Byer, S. *Gully Mapping and Drivers in the Grazing Lands of the Burdekin Catchment*; Rp66g Synthesis Report; The State of Queensland (Department of Science, Information Technology, Innovation and the Arts): Brisbane, Australia, 2014.
77. Wilkinson, S.N.; Dougall, C.; Kinsey-Henderson, A.E.; Searle, R.; Ellis, R.; Bartley, R. Development of a time-stepping sediment budget model for assessing land use impacts in large river basins. *Sci. Total Environ.* **2014**, *468–469*, 1210–1224. [[CrossRef](#)] [[PubMed](#)]
78. Goodwin, N.R.; Armston, J.D.; Muir, J.; Stiller, I. Monitoring gully change: A comparison of airborne and terrestrial laser scanning using a case study from Aratula, Queensland. *Geomorphology* **2017**, *282*, 195–208. [[CrossRef](#)]
79. Shellberg, J.G.; Brooks, A.P.; Spencer, J.; Ward, D. The hydrogeomorphic influences on alluvial gully erosion along the Mitchell River fluvial megafan. *Hydrol. Process.* **2013**, *27*, 1086–1104. [[CrossRef](#)]

80. Hancock, G.R.; Evans, K.G. Gully position, characteristics and geomorphic thresholds in an undisturbed catchment in northern Australia. *Hydrol. Process.* **2006**, *20*, 2935–2951. [[CrossRef](#)]
81. Bartley, R.; Croke, J.; Bainbridge, Z.T.; Austin, J.M.; Kuhnert, P.M. Combining contemporary and long-term erosion rates to target erosion hot-spots in the Great Barrier Reef, Australia. *Anthropocene* **2015**, *10*, 1–12. [[CrossRef](#)]
82. Isbell, R.F. *The Australian Soil Classification*; CSIRO Publishing: Collingwood, Australia, 1996.
83. Bartley, R.; Corfield, J.P.; Abbott, B.N.; Hawdon, A.A.; Wilkinson, S.N.; Nelson, B. Impacts of improved grazing land management on sediment yields, part 1: Hillslope processes. *J. Hydrol.* **2010**, *389*, 237–248. [[CrossRef](#)]
84. Gilad, U.; Denham, R.; Tindall, D. Gullies, google earth and the Great Barrier Reef: A remote sensing methodology for mapping gullies over extensive areas. In Proceedings of the International Archives of the Photogrammetry, Remote Sensing and Spatial Information Science, XXII ISPRS Congress, Melbourne, Australia, 25 August–1 September 2012; Volume XXXIX-B8, pp. 469–473.
85. Wilkinson, S.N.; Kinsey-Henderson, A.E.; Hawdon, A.A.; Ellis, T.W.; Nicholas, D.M. *Gully Erosion and Its Response to Grazing Practices in the Upper Burdekin Catchment. A Report to nq Dry Tropics for the Paddock to Reef Program*; CSIRO Water for a Healthy Country Flagship: Canberra, Australia, 2013.
86. Petheram, C.; McMahon, T.A.; Peel, M.C. Flow characteristics of rivers in northern Australia: Implications for development. *J. Hydrol.* **2008**, *357*, 93–111. [[CrossRef](#)]
87. Nicholls, N. The el niño/southern oscillation and Australian vegetation. *Vegetatio* **1991**, *91*, 23–36. [[CrossRef](#)]
88. Jarihani, B.; Sidle, R.C.; Bartley, R.; Roth, C.H.; Wilkinson, S.N. Characterisation of hydrological response to rainfall at multi spatio-temporal scales in savannas of semi-arid Australia. *Water* **2017**, *9*, 540. [[CrossRef](#)]
89. Mott, J.J.; Williams, J.; Andrew, M.H.; Gillison, A.N. Chapter 7: Australian savanna ecosystems. In *Ecology and Management of the World's Savannas*; Tothill, J.C., Mott, J.J., Eds.; Australian Academy of Sciences: Canberra, Australia, 1985; pp. 56–82.
90. Williams, R.J.; Cook, G.D.; Gill, A.M.; Moore, P.H.R. Fire regime, fire intensity and tree survival in a tropical savanna in northern Australia. *Aust. J. Ecol.* **1999**, *24*, 50–59. [[CrossRef](#)]
91. Williams, R.; Gill, A.; Moore, P. Seasonal changes in fire behaviour in a tropical savanna in northern Australia. *Int. J. Wildland Fire* **1998**, *8*, 227–239. [[CrossRef](#)]
92. Townsend, S.A.; Douglas, M.M. The effect of three fire regimes on stream water quality, water yield and export coefficients in a tropical savanna (northern Australia). *J. Hydrol.* **2000**, *229*, 118–137. [[CrossRef](#)]
93. Wilkinson, S.N.; Kinsey-Henderson, A.E.; Hawdon, A.A.; Hairsine, P.B.; Bartley, R.; Baker, B. Gully erosion processes, dynamics and controls in a tropical savannah. *Earth Surf. Process. Landf.* **2017**. under review.
94. Sibson, R. A brief description of natural neighbor interpolation. In *Interpolating Multivariate Data*; Barnett, V., Ed.; John Wiley & Sons: West Sussex, UK, 1981; pp. 21–36.
95. Dà-Jiāng Innovations Science and Technology Co (DJI). *Phantom 3 Professional User Manual v1.8*; DJI: Shenzhen, China, 2016.
96. Maps Made Easy. Maps made easy-home. Available online: <https://www.mapsmadeeasy.com/> (accessed on 3 March 2017).
97. AgiSoft LLC. Agisoft Photoscan Professional v1.3 User Manual. Available online: <http://www.agisoft.com/downloads/user-manuals/> (accessed on 3 March 2017).
98. Lowe, D.G. Distinctive image features from scale-invariant keypoints. *Int. J. Comput. Vis.* **2004**, *60*, 91–110. [[CrossRef](#)]
99. Girardeau-Montaut, D. Cloudcompare: 3D Point Cloud and Mesh Processing Software, v2.8. Available online: <http://www.danielgm.net/cc/> (accessed on 3 March 2017).
100. Geoscience Australia. Ausgeoid09. Available online: <http://www.ga.gov.au/ausgeoid/nvalcomp.jsp> (accessed on 3 March 2017).
101. Cook, K.L. An evaluation of the effectiveness of low-cost uavs and structure from motion for geomorphic change detection. *Geomorphology* **2017**, *278*, 195–208. [[CrossRef](#)]
102. Carrivick, J.L.; Smith, M.W.; Quincey, D.J. Quality assessment. In *Structure from Motion in the Geosciences*; John Wiley & Sons, Ltd: West Sussex, UK, 2016; pp. 97–123.
103. Tonkin, T.N.; Midgley, N.G.; Graham, D.J.; Labadz, J.C. The potential of small unmanned aircraft systems and structure-from-motion for topographic surveys: A test of emerging integrated approaches at cwm idwal, north Wales. *Geomorphology* **2014**, *226*, 35–43. [[CrossRef](#)]

104. Kaiser, A.; Neugirg, F.; Rock, G.; Müller, C.; Haas, F.; Ries, J.; Schmidt, J. Small-scale surface reconstruction and volume calculation of soil erosion in complex moroccan gully morphology using structure from motion. *Remote Sens.* **2014**, *6*, 7050–7080. [CrossRef]
105. Castillo, C.; Pérez, R.; James, M.R.; Quinton, J.N.; Taguas, E.V.; Gómez, J.A. Comparing the accuracy of several field methods for measuring gully erosion. *Soil Sci. Soc. Am. J.* **2012**, *76*. [CrossRef]
106. Bartley, R.; Goodwin, N.; Henderson, A.E.; Hawdon, A.; Tindall, D.; Wilkinson, S.N.; Baker, B. *A Comparison of Tools for Monitoring and Evaluating Channel Change*; Report to the national environmental science programme; Reef and Rainforest Research Centre Limited: Cairns, Australia, 2016.
107. Civil Aviation Safety Authority. Flying Drones/Remotely Piloted Aircraft in Australia. Available online: <https://www.casa.gov.au/aircraft/landing-page/flying-drones-australia> (accessed on 7 May 2017).
108. Jarihani, A.A.; Callow, J.N.; McVicar, T.R.; Van Niel, T.G.; Larsen, J.R. Satellite-derived digital elevation model (dem) selection, preparation and correction for hydrodynamic modelling in large, low-gradient and data-sparse catchments. *J. Hydrol.* **2015**, *524*, 489–506. [CrossRef]
109. Cunliffe, A.M.; Brazier, R.E.; Anderson, K. Ultra-fine grain landscape-scale quantification of dryland vegetation structure with drone-acquired structure-from-motion photogrammetry. *Remote Sens. Environ.* **2016**, *183*, 129–143. [CrossRef]
110. Brodu, N.; Lague, D. 3D terrestrial lidar data classification of complex natural scenes using a multi-scale dimensionality criterion: Applications in geomorphology. *ISPRS J. Photogramm. Remote Sens.* **2012**, *68*, 121–134. [CrossRef]
111. Jensen, J.; Mathews, A. Assessment of image-based point cloud products to generate a bare earth surface and estimate canopy heights in a woodland ecosystem. *Remote Sens.* **2016**, *8*, 50. [CrossRef]
112. Serifoglu, C.; Gungor, O.; Yilmaz, V. Performance evaluation of different ground filtering algorithms for uav-based point clouds. *Int. Arch. Photogramm. Remote Sens. Spat. Inf. Sci.* **2016**, *41*. [CrossRef]
113. Dandois, J.P.; Ellis, E.C. High spatial resolution three-dimensional mapping of vegetation spectral dynamics using computer vision. *Remote Sens. Environ.* **2013**, *136*, 259–276. [CrossRef]
114. Tonkin, T.; Midgley, N. Ground-control networks for image based surface reconstruction: An investigation of optimum survey designs using uav derived imagery and structure-from-motion photogrammetry. *Remote Sens.* **2016**, *8*, 786. [CrossRef]
115. James, M.R.; Robson, S. Mitigating systematic error in topographic models derived from uav and ground-based image networks. *Earth Surf. Process. Landf.* **2014**, *39*, 1413–1420. [CrossRef]
116. Clapuyt, F.; Vanacker, V.; Van Oost, K. Reproducibility of uav-based earth topography reconstructions based on structure-from-motion algorithms. *Geomorphology* **2016**, *260*, 4–15. [CrossRef]
117. Eltner, A.; Schneider, D. Analysis of different methods for 3D reconstruction of natural surfaces from parallel-axes uav images. *Photogramm. Rec.* **2015**, *30*, 279–299. [CrossRef]
118. Nex, F.; Remondino, F. Uav for 3D mapping applications: A review. *Appl. Geomat.* **2014**, *6*, 1–15. [CrossRef]
119. Vautherin, J.; Rutishauser, S.; Schneider-Zapp, K.; Choi, H.F.; Chovancova, V.; Glass, A.; Strecha, C. Photogrammetric accuracy and modeling of rolling shutter cameras. *ISPRS Ann. Photogramm. Remote Sens. Spat. Inf. Sci.* **2016**, *3*, 139–146. [CrossRef]

